The fracture toughness of planar lattices: imperfection sensitivity

Naomi E.R. Romijn, Norman A. Fleck *

Cambridge University Engineering Department, Trumpington Street, Cambridge CB2 1PZ, UK

Abstract

The imperfection sensitivity of in-plane modulus and fracture toughness is explored for five morphologies of 2D lattice: the isotropic triangular, hexagonal and Kagome lattices, and the orthotropic 0/90° and ±45° square lattices. The elastic lattices fail when the maximum local tensile stress at any point attains the tensile strength of the solid. The assumed imperfection comprises a random dispersion of the joint position from that of the perfect lattice. Finite element simulations reveal that the knockdown in stiffness and toughness are sensitive to the type of lattice: the Kagome and square lattices are the most imperfection sensitive. Analytical models are developed for the dependence of mode I and mode II fracture toughness of the 0/90° and ±45° lattices upon relative density. These models explain why the mode II fracture toughness of the 0/90° lattice has an unusual functional dependence upon relative density.

Key words: A. fracture toughness, microstructures, B. crack mechanics, elastic material, C. finite elements

* *Email address:* naf1@eng.cam.ac.uk (Norman A. Fleck).

1 Introduction

There is current interest in the design and use of new architectures of lattice materials for structural application, such as the core of a sandwich panel. These materials offer significant advantages over foams due to the increased nodal connectivity and the realisation of an almost perfect microstructure. In order for lattice materials to be adopted in practical engineering structures, an understanding of their defect tolerance is required. In an initial study, Fleck and Qiu (2007) assessed the fracture toughness of isotropic, two dimensional (2D) lattices made from elastic-brittle bars. They considered hexagonal and triangular honeycombs and Kagome lattices, and found that the fracture toughness K_{IC} of the 2D lattices scales with relative density $\overline{\rho}$ according to

$$\frac{K_{\mathrm{IC}}}{\sigma_f\sqrt{\ell}} = D\overline{\rho}^d \tag{1}$$

Here, σ_f and ℓ are the failure strength of the bar material and the bar length, respectively. The pre-exponent D is on the order of unity while the exponent d equals one half for the Kagome lattice, unity for the triangular honeycomb and equals two for the hexagonal honeycomb. It is emphasized that the value of this exponent has a dominant influence on the magnitude of the fracture toughness. For example, at a relative density $\overline{\rho}$ of 1%, the fracture toughness of the Kagome lattice is three orders of magnitude greater than that of the hexagonal honeycomb. But all of this is for perfect lattices. In the current study the knockdown in fracture toughness due to microstructural imperfections is addressed for a square lattice and also for the three isotropic lattices investigated by Fleck and Qiu (2007).

In a parallel study, Symons and Fleck (2007) have explored the imperfection sensitivity of the elastic moduli of hexagonal, triangular and Kagome lattices. They showed that Kagome lattices, while structurally efficient in the perfect state, are highly sensitive to imperfections. In contrast, the in-plane moduli of triangular honeycombs are almost imperfection insensitive. The hexagonal honeycomb has the unusual property that its in-plane bulk modulus is highly imperfection sensitive, whereas its shear modulus is almost insensitive to imperfection, see for example Chen et al. (1999) and Gibson and Ashby (1997).

Choi and Sankar (2005) have recently investigated the mode I and mode II fracture toughnesses of the perfect three dimensional (3D) cubic lattice. This lattice can be considered as a stack of 2D square grids, with the nodes of each grid fastened to the next layer by out-of-plane bars. Choi and Sankar explored the sensitivity of fracture toughness to relative density for an elastic, brittle bar material. We shall use the toughness calculations for a 2D lattice in order to make predictions for the fracture toughness of the 3D cubic lattice, and thereby compare our results with those of Choi and Sankar.

1.1 Scope of study

The aim of the current study is to explore the sensitivity of fracture toughness of elastic-brittle 2D planar lattices to imperfections in the form of displaced nodes. It is assumed that any bar fails when the maximum tensile stress at any point attains the fracture strength σ_f of the solid. Isotropic lattices (hexagonal, triangular and Kagome lattices) and orthotropic lattices (square lattices in the $0/90°$ and $\pm 45°$ orientations) are each considered, see Fig. 1.

First, the imperfection sensitivity of the elastic moduli of the lattices is determined. Second, the mode I and mode II fracture toughnesses of perfect and imperfect lattices are calculated. Simple analytical models are proposed to explain the functional dependence of fracture toughness of the perfect square lattices upon the relative density $\overline{\rho}$. These models are in the spirit of the analyses of Gibson and Ashby (1997) for the hexagonal honeycomb, and of Fleck and Qiu (2007) for the triangular and Kagome lattices.

2 Relative Density of Perfect and Imperfect Planar Lattices

Consider the perfect 2D lattice structures shown in Fig. 1. In all cases the lattices are made from linear elastic bars of uniform thickness t and length ℓ. The square lattices (Figs. 1a,b) are orthotropic whilst the Kagome lattice, triangular honeycomb and hexagonal honeycomb (Figs. 1c,d,e, respectively) are isotropic.

At sufficiently low relative density, $\overline{\rho} < 0.1$, the relation between $\overline{\rho}$ and the bar aspect ratio t/ℓ can be taken to be linear for all of the lattices in Fig. 1,

$$\overline{\rho} = A\frac{t}{\ell} \tag{2}$$

The value of the coefficient A depends upon the lattice geometry, as summarised in Table 1.

2.1 The relative density of imperfect lattices

We shall use the finite element method to explore the dependence of in-plane modulus and fracture toughness upon the random perturbation of nodal position. Random lattices are generated by moving each node by a random radial distance e along a random inclination α as shown in Fig. 1f. The random variables (e, α) are chosen such that there is a uniform probability of the perturbed node lying anywhere within a circle of radius R. Thus, the probability density function is

$$p(e, \alpha) = \frac{1}{2\pi Re} \tag{3}$$

In order to ensure no impingement of adjacent nodes we limit our attention to $0 \leq R/\ell \leq 0.5$. Examples of the random lattices as generated by this algorithm are shown in Fig. 2.

The effect of randomly moving the nodes of each lattice is to increase the average length of each bar. A straightforward geometric construction can be used to show that the average length $\overline{\ell}$ of the bars in the imperfect lattice is given by a series expansion in (R/ℓ) according to

$$\frac{\overline{\ell}}{\ell} = 1 + \frac{1}{4}\left(\frac{R}{\ell}\right)^2 + ... \tag{4}$$

Note that the relative density $\overline{\rho}$ scales with R/ℓ in an identical manner to that of $\overline{\ell}/\ell$. We shall ignore this small correction factor for $\overline{\rho}$ when presenting our results: the correction factor is only 1.0025 for $R/\ell = 0.1$ and remains negligible at 1.0625 for $R/\ell = 0.5$.

3 The In-plane Elastic Moduli of the 2D lattice

3.1 Moduli of perfect lattices

The in-plane stiffness of any 2D orthotropic solid is described by four elastic moduli: the direct modulus in two orthogonal directions, E_{11} and E_{22}, the shear modulus, G_{12} and the Poisson ratio, ν_{12}. For the square lattices considered here, symmetry dictates that $E_{11} = E_{22}$, so we need only consider the three elastic moduli E_{11}, G_{12} and ν_{12}.

For an isotropic solid the number of independent elastic constants is further reduced from three to two since

$$G_{12} = \frac{E_{11}}{2(1+\nu_{12})} \tag{5}$$

A strength-of-materials approach can be used to obtain analytic expressions for the in-plane elastic moduli of each perfect lattice of Fig. 1 as a function of relative density. The resulting analytic expressions for modulus already exist in the literature for all the lattices of Fig. 1 (see Choi and Sankar (2005), Fleck and Qiu (2007) and Gibson and Ashby (1997)). These analytical results are summarised below, in terms of the in-plane Cartesian axes (x_1, x_2) as defined in Fig. 1.

The moduli scale with the value E_s of the fully dense solid according to

$$\frac{E_{11}}{E_s} = B\overline{\rho}^b \tag{6}$$

and

$$\frac{G_{12}}{E_s} = C\overline{\rho}^c \tag{7}$$

where the coefficients B and C, and the exponents b and c, as well as the Poisson's ratio ν_{12}, depend upon the architecture as tabulated in Table 1. Values for the isotropic lattices are taken from Fleck and Qiu (2007). Those for square lattices are calculated using cantilever beam theory as described by Choi and Sankar (2005). An exponent of unity in Eq. (6) or (7) (as for perfect triangular, Kagome and 0/90° square lattices) indicates a stretching-dominated response, whilst an exponent of three (hexagonal honeycombs, perfect ±45° square lattices) indicates a bending-dominated response.

3.2 Finite Element Analysis of the Effective Moduli of Perfect and Imperfect Lattices

Finite Element (FE) models have been constructed for the perfect and imperfect lattices using the commercial programme ABAQUS/Standard (version 6.5). The programme was used to calculate both the effective in-plane moduli and the fracture toughness. Each bar of the lattice was treated as an Euler-Bernoulli ('B21') beam element. A cubic shape function was sufficient to model the transverse beam displacement associated with a linear bending distribution along each beam.

The effective macroscopic properties were determined using periodic cell simulations of side length 200ℓ by 200ℓ. Periodic boundary conditions on displacement were applied such that an average strain was imposed on the overall mesh. A preliminary mesh convergence study revealed that this mesh is of adequate size to give repeatable results. In order to assess this quantitatively, five structural realisations were constructed for any given level of randomness R/ℓ of the lattice. For the mesh of size $200\ell \times 200\ell$ it was found that the scatter in moduli was less than 1% for $\overline{\rho} = 0.4$ and about 4% for $\overline{\rho} = 0.01$. This was deemed acceptable for present purposes and only the average values are given below.

3.3 The Dependence of Modulus upon Relative Density

The dependence of E_{11} and G_{12} upon $\overline{\rho}$ are shown in Figs. 3a,b for the perfect lattices (piecewise-linear solid lines) and for the lattices with the most extreme imperfection of $R/\ell = 0.5$ (piecewise-linear dotted lines). In each case, multiple simulations were performed for each of 8 selected values of $\overline{\rho}$. Straight-line fits to the log-log graphs of Fig. 3 were performed for the perfect geometries. These curve fits confirmed the accuracy of formulae (6) and (7) and the values of coefficients listed in Table 1. For example, for the hexagonal lattice a curve fit revealed that

$$\frac{E_{11}}{E_s} = 1.47\overline{\rho}^3 \tag{8}$$

The coefficient of 1.47 is within 3% of the value 3/2 given by the analytical result of Table 1. For all lattices the analytical values of the pre-exponents are within 8% of the FE values. We conclude that the formulae listed in Table 1 are adequate for our purposes.

3.3.1 Direct modulus of imperfect lattices

It is clear from Fig. 3a that the direct moduli of the hexagonal and triangular honeycombs are only mildly sensitive to imperfections: upon perturbing the nodal positions the hexagonal honeycomb remains bending-dominated while the triangular honeycomb remains stretching-dominated. However, a dispersion of nodal position for the square and Kagome lattices changes the value of the exponent in the power-law fit of modulus versus relative density.

First, consider the imperfect ($R/\ell = 0.5$) Kagome lattice. The presence of the imperfections increases the value of b to above unity: b varies from approximately 3 at low $\overline{\rho}$ (bending dominated) to 1.5 at high $\overline{\rho}$ (suggesting that the deformation mode involves a stretching component). Alternatively, a straight line fit may be used to approximate the imperfect Kagome data (Fig. 3), such that

$$\frac{E_{11}}{E_s} \approx 0.54\overline{\rho}^2. \tag{9}$$

The index of 2 is consistent with the arguments made by Wicks and Guest (2004) for the local stiffness of a Kagome lattice with an imperfection in the form of a missing bar. They show that the quadratic dependence of stiffness upon $\overline{\rho}$ is a result of combined bending and stretching in approximately equal proportions.

Second, consider the $0/90°$ square lattice. An examination of the deformed FE mesh reveals that direct loading leads to significant bending in the imperfect lattice. The drop in direct modulus can be associated with a switch in deformation mode from stretching to bending. In contrast, imperfections in the ±45° lattice lead to an increase in direct modulus by switching the deformation mode from one of bending to one of combined bending and stretching.

3.3.2 Shear modulus of imperfect lattices

Now consider the shear stiffness for an extreme imperfection $R/\ell = 0.5$ for each lattice, as shown in Fig. 3b. Nodal dispersion results in a major drop in shear modulus for the Kagome lattice, but gives only a minor change in shear modulus for the other two isotropic structures. The imperfection sensitivities are comparable for shear and direct loadings for each of the three isotropic lattices, compare Figs. 3a and 3b.

The perfect ±45° lattice deforms by bar stretching under shear loading, while the imperfect ±45° lattice deforms in a more compliant manner by a combination of bending and stretching of bars. This mimics closely the imperfection sensitivity of the 0/90° lattice to direct loading. Introduction of imperfections to the 0/90° lattice changes its shear response from one of bar bending to combined bending and stretching. Consequently, the macroscopic shear modulus increases.

A detailed treatment of the role of various imperfections (including nodal dispersion) upon the in-plane effective properties is given in the parallel study by Symons and Fleck (2007) for the three isotropic lattices. Our results presented here are consistent with their findings, and are included here in order to contrast the imperfection sensitivity of the square lattice with that of the isotropic lattices. We shall also make use of the effective moduli in our prediction of fracture toughness.

3.4 Imperfection Sensitivity of the Elastic Moduli

We proceed to explore the imperfection sensitivity of the lattices at a fixed stockiness $t/\ell = 0.01$. Figs. 4a and b show respectively the direct and shear modulus versus imperfection amplitude in the range ($0 < R/\ell < 0.5$). The vertical axes have been normalised by the moduli of the respective perfect lattices to facilitate comparison of the five lattice topologies, i.e.

$$\overline{E}_{11} = \frac{E_{11}}{E_p}\,, \qquad \overline{G}_{12} = \frac{G_{12}}{G_p} \tag{10}$$

where E_p and G_p are the (topology-specific) direct and shear moduli of the *perfect* lattices at the same t/ℓ value. The following observations may be drawn from Fig. 4.

(1) The hexagonal lattice deforms by bar bending, while the triangular lattice deforms by bar stretching, regardless of the level of imperfection. Consequently, the macroscopic moduli are almost insensitive to the magnitude of imperfection, R/ℓ.

(2) The direct modulus of the $0/90°$ square lattice and the shear modulus of the $\pm 45°$ lattice decrease almost linearly with increasing R/ℓ. This is due to the introduction of bar bending by the presence of imperfections. Likewise, the axial and shear moduli of the Kagome lattice decrease almost linearly with increasing R/ℓ.

(3) The direct modulus of the $\pm 45^\circ$ lattice and the shear modulus of the $0/90^\circ$ lattice increase in an approximately quadratic manner with increasing R/ℓ. This is associated with the observation that the perfect lattice bends while the imperfect lattice carries load by a combination of bar stretching and bar bending.

3.5 Imperfection Sensitivity of Poisson's Ratio and the Degree of Anisotropy

The Poisson ratio ν_{12} is plotted as a function of $\overline{\rho}$ in Fig. 5a for all topologies, with $R/\ell = 0$ and 0.5 In all cases, ν_{12} is almost independent of $\overline{\rho}$ for $\overline{\rho} \leq 0.01$, as expected by simple beam theory. At higher relative densities the bending and stretching stiffnesses of a beam are comparable and ν_{12} varies somewhat with $\overline{\rho}$.

The imperfection sensitivity of Poisson's ratio ν_{12} is shown in Fig. 5b for $t/\ell = 0.01$. A wide range of ν_{12} is evident, with the value dependent upon both the choice of topology and the level of imperfection. ν_{12} is insensitive to R/ℓ for the triangular and $\pm 45^\circ$ lattices. For the remaining lattices, ν_{12} decreases monotonically with increasing imperfection R/ℓ.

Now consider the dependence of the isotropy measure $I \equiv 2G_{12}(1 + \nu_{12})/E_{11}$ upon $\overline{\rho}$ and R/ℓ, see Figs. 6a and 6b, respectively. As expected, the three isotropic lattices (Kagome, triangular and hexagonal) remain isotropic when nodes are randomly displaced, and this is reflected by the result $I = 1$ regardless of the values of $\overline{\rho}$ and R/ℓ. Introduction of dispersed nodes into the orthotropic (square) lattices induces a more isotropic response and I tends towards unity with increasing R/ℓ, see Fig. 6b.

Finally, consider the dependence of I upon $\overline{\rho}$ for $R/\ell = 0$ and 0.5, as shown in Fig. 6a. The shear and axial moduli have markedly different dependences upon $\overline{\rho}$ for the two square lattices. Consequently, the value of I is sensitive to $\overline{\rho}$ for these lattices, particularly in the perfect state $R/\ell = 0$.

3.6 Plane strain moduli

So far, we have considered a 2D lattice in plane stress such that $\sigma_{33} = \sigma_{13} = \sigma_{23} = 0$, where the x_3 axis is normal to the (x_1, x_2) plane of Fig. 1. Alternatively, plane strain conditions can be envisaged such that $\varepsilon_{33} = 0$. The effective modulus in the prismatic direction is $E_{33} = \overline{\rho} E_s$, and the longitudinal Poisson ratios $\nu_{31} = \nu_{32}$ equal the value ν_s of the solid. Consequently, in plane strain we have $\sigma_{33} = \nu_s(\sigma_{11} + \sigma_{22})$. The in-plane, plane stress modulus E_{11} is now replaced by the plane strain modulus E_{11}^{ps}, and the in-plane Poisson ratio ν_{12} is replaced by the plane strain value ν_{12}^{ps}, where

$$E_{11}^{ps} = \frac{1}{1 - \nu_s^2 B \overline{\rho}^{b-1}} E_{11} \tag{11}$$

and

$$\nu_{12}^{ps} = \frac{\nu_{12} + \nu_s^2 B \overline{\rho}^{b-1}}{1 - \nu_s^2 B \overline{\rho}^{b-1}} \tag{12}$$

Plane strain moduli and Poisson ratios for the lattices of Fig. 1 are listed in Table 2, according to the above prescription. Note that the shear modulus G_{12} for plane strain is the same as that for plane stress.

It remains to compare the plane strain moduli with the plane stress values.

Consider the case $\nu_s = 0.3$ and $\overline{\rho}$ in the range 10^{-3} to 10^{-1}. The plane strain moduli for the three isotropic lattices is about 3% above the plane stress value, while the Poisson ratio increases by up to 13%. Likewise, the square lattices show only a negligible increase in their direct moduli and Poisson ratios upon switching from plane stress to plane strain.

4 Prediction of Fracture Toughness

Sih et al. (1965) have determined the K-field at the tip of a semi-infinite crack in an orthotropic elastic plate. We make extensive use of their solution in order to apply the K-field on the outer periphery of a finite element mesh containing a single edge crack, see Fig. 7. The fracture toughness of the lattice is calculated by equating the maximum tensile stress at any point in the FE mesh to the assumed tensile strength σ_f of the solid.

A finite element mesh of side length 600ℓ by 600ℓ was constructed from Euler-Bernoulli ('B21') beam elements. The mesh contains a traction free edge crack of length 300ℓ, see Fig. 7. Loading was imposed by the displacement field of the K-field on the boundary nodes of the mesh, as given by Sih et al. (1965). A mesh convergence study revealed that this mesh size is adequate for the stockiness range investigated ($0.001 \leq t/\ell \leq 0.2$). Nodal rotations equal to the material rotation of the K-field were imposed on the periphery of the mesh. The resulting fracture toughness was within 0.1% of the value obtained allowing free rotation of peripheral nodes. Thus, the precise prescription of nodal rotation on the periphery of the mesh is unimportant.

The fracture toughness of the lattices was calculated as follows. The maximum tensile stress anywhere in the structure was determined for pure mode I loading and then for pure mode II loading. The predicted macroscopic toughness K_{C} is the value of remote K at which the maximum local tensile stress attains the fracture strength σ_f. Results are presented both for the perfect topology and for the case of randomly dispersed joints (as randomised by the prescription of section 2.1). In order to minimise the scatter in results for the random structures, ten structural realisations were performed for selected values of relative density $\overline{\rho}$ and for selected values of randomness R/ℓ.

4.1 Fracture toughness of perfect lattices: FE results

The predicted mode I toughness $K_{\mathrm{IC}}/\sigma_f\sqrt{\ell}$ is plotted as a function of the relative density $\overline{\rho}$ in Fig. 8a for each topology. Similarly, the mode II fracture toughness $K_{\mathrm{IIC}}/\sigma_f\sqrt{\ell}$ is given in Fig. 8b. The plots include results for the perfect topologies $R/\ell = 0$ (shown as solid lines), and also for the case of an extreme imperfection $R/\ell = 0.5$ (dotted lines). The fracture toughness drops significantly with increasing R/ℓ for all lattices except the hexagonal honeycomb; this topology has a low toughness which is relatively insensitive to imperfections. We save our full discussion of the imperfect lattices to section 4.4.

It is seen from Fig. 8 that the fracture toughness K_{C} has a power-law dependence upon $\overline{\rho}$, such that

$$\frac{K_{\mathrm{C}}}{\sigma_f\sqrt{\ell}} = D\overline{\rho}^d \qquad (13)$$

where the values of (D, d) depend upon both the topology and the degree of imperfection. Curve fits have been performed on the data shown in Fig. 8, and the values of (D, d) for the perfect lattices are listed in Table 3. The exponent d ranges from 0.5 for the mode I and mode II toughness of the perfect Kagome lattice to the value of 2 for the mode I and mode II toughness of the hexagonal honeycomb, as already remarked upon by Fleck and Qiu (2007).

The triangular honeycomb and the $\pm 45^\circ$ lattice are intermediate structures in the sense that the mode I and mode II fracture toughnesses scale linearly with $\overline{\rho}$. A more complex behaviour is noted for the $0/90^\circ$ lattice: K_{IC} scales linearly with $\overline{\rho}$ for mode I, while K_{IIC} scales as $\overline{\rho}^{3/2}$.

Analytical models for the mode I and mode II toughness of the three isotropic, perfect lattices have already been given by Fleck and Qiu (2007) and Gibson and Ashby (1997). These models give the correct values for the exponent d, and accurate estimates for D. In the following section, models are constructed for the toughness of the $0/90^\circ$ and $\pm 45^\circ$ perfect square lattices.

4.2 Analytical models for the fracture toughness of the perfect square lattices

Consider an edge crack in an orthotropic plate, as shown in Fig. 7. Write the displacement field in Cartesian form as u_i^{I} for a mode I crack, and as u_i^{II} for a mode II crack. Then introduce the polar co-ordinates (r, θ) centred on the crack tip, with the crack faces lying along the $\theta = \pm\pi$ rays, as sketched in Fig. 7. The displacement field of the K field in an orthotropic plate is given by Sih et al. (1965), and is of the form

$$u_i^{\mathrm{I}}(r,\theta) = \frac{K_{\mathrm{I}}\sqrt{r}}{E_s} f_i^{\mathrm{I}}(\theta,\overline{\rho}) \tag{14}$$

for mode I, and

$$u_i^{\mathrm{II}}(r,\theta) = \frac{K_{\mathrm{II}}\sqrt{r}}{E_s} f_i^{\mathrm{II}}(\theta,\overline{\rho}) \tag{15}$$

for mode II. The non-dimensional functions $f_i^{\mathrm{I}}(\theta,\overline{\rho})$ and $f_i^{\mathrm{II}}(\theta,\overline{\rho})$ depend upon the angular co-ordinate θ and upon the orthotropic properties of the plate. The dependence upon $\overline{\rho}$ enters because the ratio of shear modulus to direct modulus is a function of $\overline{\rho}$, see Eqs. (6) and (7).

An analytical model for the macroscopic fracture toughness is now estimated by considering the stress state within the critical bar of the lattice. The location of maximum tensile stress depends upon the mode mix and upon the orientation of the lattice, and is marked by a small circle on the deformed meshes shown in Figs. 9a-d.

Consider first the case of a $\pm 45°$ lattice under mode I loading. The critical bar is at the crack tip, and the maximum tensile stress in this bar is determined in the manner as described by Quintana Alonso and Fleck (2007). Assume that the critical bar deforms as a built-in cantilever beam, see Fig. 10. The clamping moment M on this bar is

$$M = \frac{1}{2} E_s \frac{t^3}{\ell^2} u_T \tag{16}$$

in terms of the transverse displacement, u_T, as shown in Fig. 10. Now u_T scales with the crack tip opening displacement, δ, evaluated at a distance $x' = \ell/\sqrt{2}$ behind the crack tip, according to

$$u_T = \frac{\delta(x' = \ell/\sqrt{2})}{2\sqrt{2}} \tag{17}$$

Recall that the crack tip opening of an orthotropic continuum is given by

$$\delta(x') = \frac{8}{\sqrt{2\pi}} C K_{\mathrm{I}} \sqrt{x'} \tag{18}$$

where the elastic coefficient C depends upon the degree of orthotropy (Sih et al., 1965; Tada et al., 1985). For the $\pm 45°$ square lattice we have

$$C = \frac{2\sqrt{2}}{\overline{\rho}^2 E_s} \tag{19}$$

Assume that the critical beam of Fig. 10 fails when the local bending stress $\sigma = 6M/t^2$ attains the tensile fracture strength σ_f of the bar material. Now make use of Eqs. (16)-(19) and the geometric relation $\overline{\rho} = 2t/\ell$ in order to obtain

$$K_{\mathrm{IC}} = 2^{-1/4} \, \frac{\sqrt{\pi}}{6} \, \overline{\rho} \, \sigma_f \sqrt{\ell} \tag{20}$$

A similar argument may be developed for the $\pm 45°$ lattice under remote mode II loading, and for the the $0/90°$ lattice under mode I loading. Expressions (18) and (19) remain valid, with no change of numerical constants. The values of fracture toughness follow immediately as

$$K_{\text{IIC}} = 2^{-1/4}\,\frac{\sqrt{\pi}}{6}\,\overline{\rho}\,\sigma_f\sqrt{\ell} \tag{21}$$

for the ±45° lattice under mode II loading, and

$$K_{\text{IC}} = \frac{1}{6}\sqrt{\frac{\pi}{2}}\,\overline{\rho}\,\sigma_f\sqrt{\ell} \tag{22}$$

for the 0/90° lattice under mode I loading. Expressions (20), (21) and (22) are in excellent agreement with the finite element predictions listed in Table 3: there is only a slight discrepancy in the numerical constant.

4.2.1 Mode II fracture toughness of a 0/90° lattice

Now consider the remaining case of a 0/90° lattice under mode II loading. The procedure outlined in the previous section would erroneously predict that the fracture toughness K_{IIC} scales linearly with $\overline{\rho}$. In reality, the finite element simulations of the discrete lattice reveal that K_{IIC} scales as $\overline{\rho}^{3/2}$. The discrepancy can be traced to the difference in crack face sliding displacements of the two solutions: the displacement scales as $\overline{\rho}^{-2}$ in the orthotropic continuum solution while it scales as $\overline{\rho}^{-5/2}$ for the discrete lattice. Further investigation revealed that the displacement field in the continuum solution has a steep variation in the vicinity of the crack flanks, particularly at low $\overline{\rho}$, fand this small sector of intense strain does not exist in the discrete lattice. This 'boundary layer' is explored further below.

The orthotropic continuum solution for the near tip displacement u_1 in the x_1-direction is plotted in Fig. 11 as a function of the shifted polar co-ordinate $\theta' = \pi - \theta$ at fixed radius r. Upon normalising the displacement u_1 by $\overline{\rho}^{5/2}$ it is seen that the displacement field has a converged solution for a wide range of $\overline{\rho}$ at $\theta' > \pi/4$. Recall that this scaling is the same as that exhibited by the discrete lattice solution. In contrast, the crack face displacement of the continuum scales as $\overline{\rho}^{-2}$ and so the normalisation $u_1\overline{\rho}^{5/2}$ is inappropriate in the limit $\theta' \rightarrow 0$. Thus, the normalised curves for u_1 in Fig. 11 diverge as $\theta' \rightarrow 0$.

It is instructive to add to this plot the finite element solution for u_1 at $r = \ell/2$ and $\theta' = 0$ *for the discrete lattice*. Note that the crack faces of the discrete lattice (along $\theta' = 0$) displace by a similar amount to that of the continuum solution at $\pi/4 < \theta' < 3\pi/4$. In contrast, the crack face displacement of the discrete lattice is significantly greater than that of the continuum solution.

A simple analytical model can now be developed for the mode II toughness of a discrete 0/90° lattice. Recall that the critical bar lies directly ahead of the crack tip, see Fig. 9d. This bar behaves as a clamped-clamped beam, with relative displacement Δu across its ends. We argue that Δu is given by the crack sliding displacement at $r = \ell/2$ and $\theta' = 0$ for the discrete 0/90° lattice. This displacement is shown in Fig. 11 and is given by

$$\Delta u = 2u_1 = 14.1 \frac{K_{\mathrm{II}}\sqrt{\ell}}{E_s \overline{\rho}^{2.5}} \tag{23}$$

according to the finite element solution. We have already remarked that the orthotropic continuum solution can be used to obtain this displacement, provided we take the solution for $\pi/4 < \theta' < 3\pi/4$. To complete the model, we invoke equation (16) and the beam bending formula $\sigma = 6M/t^2$ as before, and thereby obtain

$$K_{\mathrm{IIC}} = 0.047\overline{\rho}^{1.5}\sigma_f\sqrt{\ell} \tag{24}$$

This is in reasonable agreement with the values for (D, d) as listed in Table 3 from the full finite element simulations. The exponent d is precise, while the pre-exponent D is given only approximately by the analytical model.

4.2.2 Shear lag region

The 0/90°, ±45° and Kagome lattices each exhibit narrow shear bands emanating from the crack tip along the principal material directions: the bars traversing the shear band are subjected to a high bending moment. We define the length of the shear lag region L as the distance over which the bending moment M within the shear band drops to 10% of the value M_0 at the crack tip, as shown in Fig. 12a.

The length of the shear lag region is plotted against relative density $\overline{\rho}$ in Fig. 12b. Using this criterion, the length of the shear lag region in a 0/90° square lattice under mode I loading is $L/\ell \approx 2/\overline{\rho}$. Using the same criterion for mode I loading of a ±45° lattice, we have $L/\ell \approx 50/\overline{\rho}$. Note that, using this criterion, the length of the shear lag region exceeds the mesh size for $\overline{\rho} < 0.1$.

The size L of the shear lag region in the Kagome lattice scales as $L/\ell \approx 0.1/\overline{\rho}$. However, for $\overline{\rho} \geq 0.1$, the shear lag region spans only a few cells, and its length becomes independent of relative density, see Fig. 12b. The hexagonal honeycomb is a bending dominated structure, and hence bending is not restricted to a shear lag region: the concept of a shear lag region does not apply. Similarly, no shear lag region is observed in the stretching dominated triangular lattice as bars carry axial loads rather than bending loads.

4.3 Fracture toughness of a 3D Cubic Lattice

For a planar 0/90° square lattice, we have found that the 2D fracture toughness $K_{\mathrm{C}}^{(\mathrm{2D})}$ is

$$K_{\mathrm{C}}^{(\mathrm{2D})} = D\,\overline{\rho}^{\,d}\,\sigma_f\sqrt{\ell} \tag{25}$$

with $(D, d) = (0.278, 1)$ under mode I loading, and $(D, d) = (0.121, 1.5)$ under mode II loading. We can make use of this result in order to predict the fracture toughness of a 3D simple cubic lattice. The unit cell of the cubic lattice has side length ℓ and is composed of bars of square cross-section $t \times t$. This 3D lattice can be considered to comprise a separated stack of 2D square grids each of thickness t. One grid is fastened to the next layer at its nodes by out-of-plane bars of length ℓ. The fracture toughness of the 3D lattice $K_{\mathrm{C}}^{(\mathrm{3D})}$ is then related to the fracture toughness of the 2D lattice $K_{\mathrm{C}}^{(\mathrm{2D})}$ by

$$K_{\mathrm{C}}^{(\mathrm{3D})} = \frac{t}{\ell} K_{\mathrm{C}}^{(\mathrm{2D})} \tag{26}$$

It remains to express $K_{\mathrm{C}}^{(\mathrm{3D})}$ in terms of the relative density $\rho^*/\rho_s = 3(t/\ell)^2$ for the 3D lattice. Recall that $\overline{\rho} = 2t/\ell$ for the 2D lattice, and upon substituting equation (25) into (26) we obtain

$$K_{\mathrm{C}}^{(3\mathrm{D})} = D' \left(\frac{\rho^*}{\rho_s}\right)^{d'} \sigma_f \sqrt{\ell} \tag{27}$$

where

$$D' = \frac{2^d\, D}{3^{\frac{d+1}{2}}} \tag{28}$$

and

$$d' = \frac{d+1}{2} \tag{29}$$

The so-obtained values of (D', d') for mode I and II loading are given in the first row of Table 4. Note that d' equals unity for mode I and 5/4 for mode II.

Choi and Sankar (2005) have recently investigated the mode I and mode II fracture toughnesses of the perfect 3D cubic lattice. They explored the sensitivity of fracture toughness to relative density for an elastic, brittle solid of density $\rho_s = 1750$ kg/m^3, Young's modulus $E_s = 207$ GPa and ultimate tensile strength of $\sigma_f = 3.6$ GPa. It is instructive to compare our results with theirs.

Choi and Sankar (2005) did not make use of dimensional analysis and first chose to vary t for a fixed cell size $\ell = 200\ \mu$m, giving

$$K_{\mathrm{IC}} = 1.961 \left(\frac{\rho^*}{\rho_s}\right)^{1.045} \mathrm{MPa}\sqrt{\mathrm{m}} \tag{30}$$

$$K_{\mathrm{IIC}} = 6.95 \left(\frac{\rho^*}{\rho_s}\right)^{1.32} \mathrm{MPa}\sqrt{\mathrm{m}} \tag{31}$$

Second, they varied the cell size ℓ at a fixed bar thickness of $t = 20$ μm and obtained

$$K_{\mathrm{IC}} = 7.82 \left(\frac{\rho^*}{\rho_s}\right)^{0.788} \ \mathrm{MPa}\sqrt{\mathrm{m}} \tag{32}$$

$$K_{\mathrm{IIC}} = 2.76 \left(\frac{\rho^*}{\rho_s}\right)^{1.07} \ \mathrm{MPa}\sqrt{\mathrm{m}} \tag{33}$$

Values of (D', d') have been extracted from these expressions, and are presented in Table 4. There is reasonable agreement between their predicted values of d' and those obtained in the present study.

It is of concern that Choi and Sankar found values of D' which varied by an order of magnitude depending upon whether they varied t or ℓ. Dimensional analysis tells us that the result is unique. Their mode II results do not show this inconsistent behaviour. We believe that the results of the present study are more accurate as the mesh size employed is much greater than that used by Choi and Sankar (2005).

4.4 Fracture Toughness of Imperfect 2D Lattices

The sensitivity of fracture toughness to nodal dispersion is now addressed for the 2D lattices shown in Fig. 1. Define the normalised mode I fracture toughness for any lattice by

$$\overline{K}_{\mathrm{IC}} = \frac{K_{\mathrm{IC}}(R/\ell)}{K_{\mathrm{IC}}(0)} \tag{34}$$

where $K_{\rm IC}(R/\ell)$ is the mode I fracture toughness of the imperfect lattice and $K_{\rm IC}(0)$ is the mode I fracture toughness of the perfect lattice of the same topology and relative density. Significant scatter was observed in the predicted fracture toughness: the standard deviation increases with R/ℓ to a value of approximately 20% of the mean value for $R/\ell = 0.5$. This scatter is a consequence of the use of a local fracture criterion in the random mesh rather than a more global, averaged criterion. We adopt the pragmatic approach of presenting the average results from 10 simulations for each topology, slenderness and value of R/ℓ.

4.4.1 Fracture toughness of imperfect lattices

Consider again Fig. 8, which shows the fracture toughness of perfect and imperfect lattices as a function of relative density. Introduction of an extreme imperfection ($R/\ell = 0.5$) causes the Mode I and Mode II fracture toughnesses of the square and Kagome lattices to drop to almost that of the perfect hexagonal honeycomb, with an exponent d of 2. For a slenderness ratio $t/\ell = 0.001$ this drop is large: by a factor of up to 3×10^4 for the case of the Kagome lattice. In contrast, the fracture toughnesses of the hexagonal honeycomb is almost insensitive to imperfection. Imperfections in the triangular honeycomb lead to a small drop in fracture toughness: this is discussed in more detail in the following section.

4.4.2 Imperfection sensitivity of fracture toughness

The normalised mode I fracture toughness, $\overline{K}_{\rm IC}$ as defined in Eq. (34) is plotted against the degree of imperfection R/ℓ in Fig. 13a for all five lattices and

$t/\ell = 0.01$. Ten structural realisations are considered for each R/ℓ, and the mean response is shown by a solid line in the figure. Significant scatter is evident. The mode I fracture toughness decreases with increasing R/ℓ for all lattice topologies, with extreme sensitivity exhibited by the Kagome, $\pm 45^\circ$ and $0/90^\circ$ lattices.

For example, introduction of an imperfection $R/\ell = 0.1$ into the Kagome lattice results in a decrease of fracture toughness by a factor of approximately three. The hexagonal and triangular honeycombs are only slightly sensitive to R/ℓ: $\overline{K}_{\mathrm{IC}}$ decreases linearly with increasing R/ℓ, and for an extreme imperfection of $R/\ell = 0.5$ the mode I fracture toughness $\overline{K}_{\mathrm{IC}}$ takes values of 0.7 and 0.4, respectively.

The normalised mode II fracture toughness, $\overline{K}_{\mathrm{IIC}}$ is defined as

$$\overline{K}_{\mathrm{IIC}} = \frac{K_{\mathrm{IIC}}(R/\ell)}{K_{\mathrm{IIC}}(0)} \tag{35}$$

where $K_{\mathrm{IIC}}(R/\ell)$ is the mode II fracture toughness of the imperfect lattice and $K_{\mathrm{IIC}}(0)$ is the mode II fracture toughness of the perfect lattice of the same topology and relative density. $\overline{K}_{\mathrm{IIC}}$ is plotted against the level of imperfection R/ℓ in Fig. 13b. Note that, for the $0/90^\circ$ square lattice and the hexagonal honeycomb, the mode II toughness is essentially insensitive to the degree of imperfection. Although the average value of fracture toughness $\overline{K}_{\mathrm{IIC}}$ is approximately unity for these two cases, there is a high degree of scatter. This is a consequence of the sensitivity of stress state near the crack tip to the precise structural geometry there.

The imperfection sensitivities of the mode II fracture toughness of the triangular honeycomb, the $\pm 45^\circ$ square lattice and the Kagome lattice are very similar to the mode I fracture toughness sensitivities.

4.4.3 Comparison of the imperfection sensitivities of moduli and fracture toughness

The imperfection sensitivity of the mode I and mode II fracture toughness, $\overline{K}_{\mathrm{I}}$ and $\overline{K}_{\mathrm{II}}$ is compared in Fig. 14 with that of the Young's modulus $\overline{E}_{11}$ and shear modulus $\overline{G}_{12}$ for each lattice topology.

Consider first the Kagome lattice imperfection sensitivity, see Fig. 14c. All four quantities ($\overline{E}_{11}$, $\overline{G}_{12}$, $\overline{K}_{\mathrm{I}}$ and $\overline{K}_{\mathrm{II}}$) exhibit similar, high imperfection sensitivities. For the triangular honeycomb (Fig. 14d), the elastic moduli reduce gradually and in a linear manner with increasing R/ℓ. The fracture toughness also drops in an almost linear manner, but at a somewhat faster rate.

The results for a hexagonal honeycomb are shown in Fig. 14e. All four quantities are largely insensitive to the degree of imperfection. The elastic moduli and $\overline{K}_{\mathrm{II}}$ increase slightly with increasing R/ℓ, while $\overline{K}_{\mathrm{I}}$ drops almost linearly with increasing R/ℓ.

It remains to discuss the imperfection sensitivity of the $0/90^\circ$ and $\pm 45^\circ$ square lattices, plotted in Figs. 14a and 14b, respectively. The imperfection sensitivities of $\overline{K}_{\mathrm{I}}$ and the direct modulus $\overline{E}_{11}$ are similar for the $0/90^\circ$ lattice, while the imperfection sensitivities of $\overline{K}_{\mathrm{II}}$ and $\overline{G}_{12}$ are similar for the $\pm 45^\circ$ lattice.

5 Concluding Remarks

The imperfection sensitivity of modulus and fracture toughness for the lattices of the present study can be catalogued in terms of the nodal connectivity of each lattice. The hexagonal honeycomb, with a connectivity of 3 bars per joint, is a bending-dominated structure and the random movement of nodes has only a small effect upon the bending stiffness of the bars and upon the stress state in the lattice. Thus, the hexagonal lattice has a low sensitivity to nodal dispersion. The triangular lattice has a high connectivity of 6 bars per joint, and is a stretching-dominated structure. Again, it is imperfection insensitive: the random movement of nodes will have only a small effect upon the stretching stiffness of the bars and upon the stress state in the lattice. But the Kagome and square lattices are transition cases, with a connectivity of 4 bars per joint. For these structures, the response can be bending or stretching dominated, depending upon the level of imperfection (and upon the loading direction in relation to the microstructure for the square lattices). Thus, the moduli and fracture toughness of these topologies are highly sensitive to imperfection.

The fracture toughness of the highly imperfect lattices ($R/\ell = 0.5$) increases with increasing connectivity, recall Fig. 8. It is remarkable that the fracture toughness of the $0/90°$, $\pm 45°$ and Kagome lattices are almost identical when the imperfection is large ($R/\ell = 0.5$). The nodal connectivity appears to dictate the response more than the precise lattice topology, compare Fig. 2a,b and c.

Analytical models are given for the fracture toughness of the $0/90°$ and $\pm 45°$

square lattices under mode I and mode II loadings. These models are instructive for explaining the power law dependence of fracture toughness upon relative density $\overline{\rho}$. It is striking that $K_{\rm IIC}$ scales as $\overline{\rho}^{1.5}$ rather than $\overline{\rho}$ for the 0/90° lattice.

References

Chen, C., Lu, T., Fleck, N., 1999. Effects of imperfections on the yielding of two-dimensional foams. Journal of the Mechanics and Physics of Solids 47 (11), 2235–2272.

Choi, S., Sankar, B., 2005. A micromechanical method to predict the fracture toughness of cellular materials. International Journal of Solids and Structures 42, 1797–1817.

Fleck, N., Qiu, X., 2007. The damage tolerance of elastic-brittle, two dimensional isotropic lattices. Journal of the Mechanics and Physics of Solids 55 (3), 562–588.

Gibson, L., Ashby, M., 1997. Cellular solids - Structure and properties. Cambridge University Press.

Quintana Alonso, I., Fleck, N., 2007. Damage tolerance of an elastic-brittle diamond-celled honeycomb. Scripta Materialia 56, 693–696.

Sih, G., Paris, P., Irwin, G., 1965. On cracks in rectilinearly anisotropic bodies. International Journal of Fracture Mechanics 1 (3), 189–203.

Symons, D., Fleck, N., 2007. A systematic comparison of the imperfection sensitivity of planar, isotropic elastic lattices. Journal of the Mechanics and Physics of Solids - in press.

Tada, H., Paris, P., Irwin, G., 1985. The stress analysis of cracks handbook. 2nd Edition.

Wicks, N., Guest, S., 2004. Single member actuation in large repetitive truss structures. International Journal of Solids and Structures 41, 965–978.

List of Figures

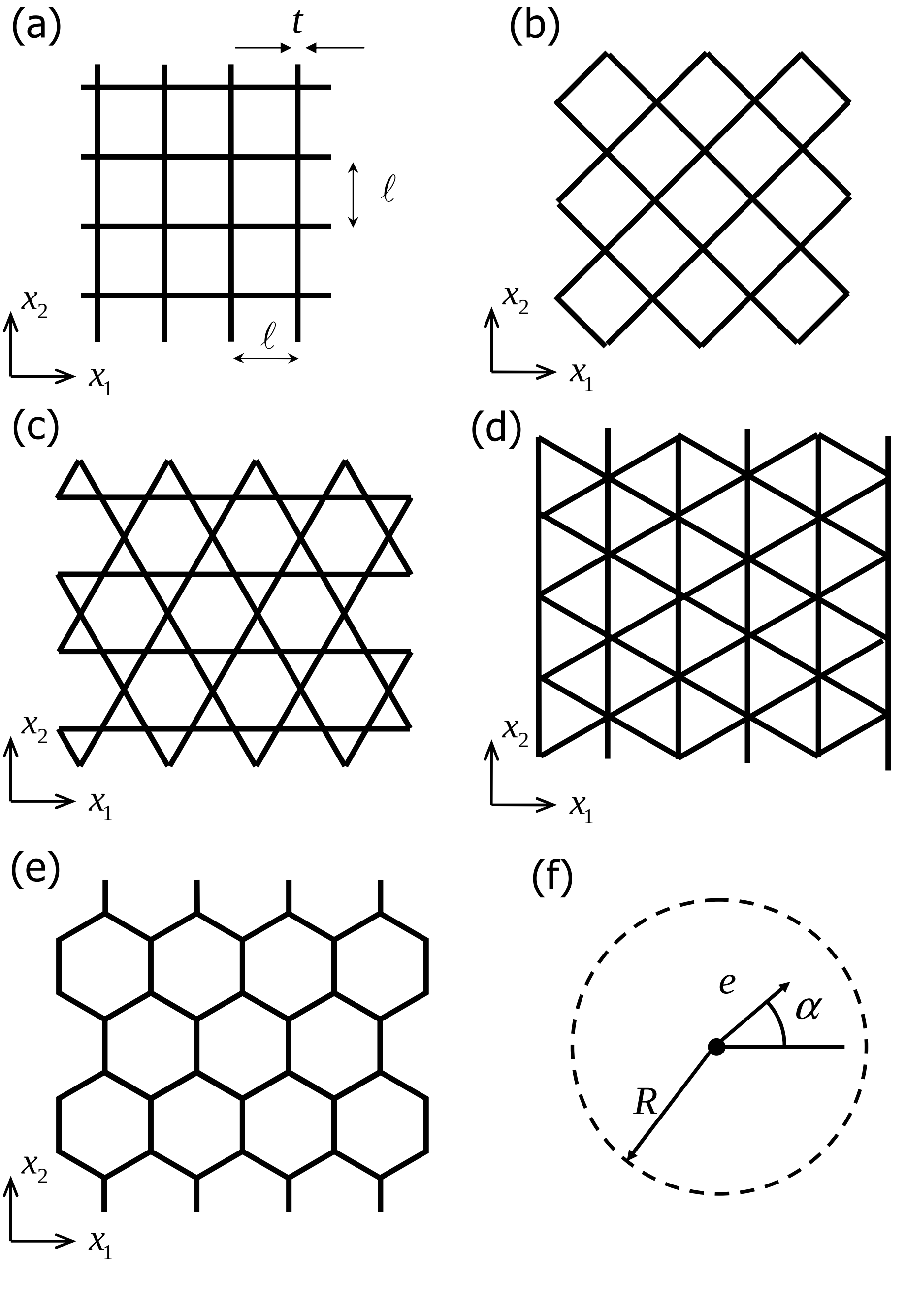

Fig. 1. (a) 0/90° square; (b) ±45° square; (c) Kagome lattice; (d) triangular honeycomb; (e) hexagonal honeycomb. (f) The geometric imperfection. Each node is perturbed by a random distance e at a random angle α. The probability density is uniform within a prescribed circular disc of radius R.

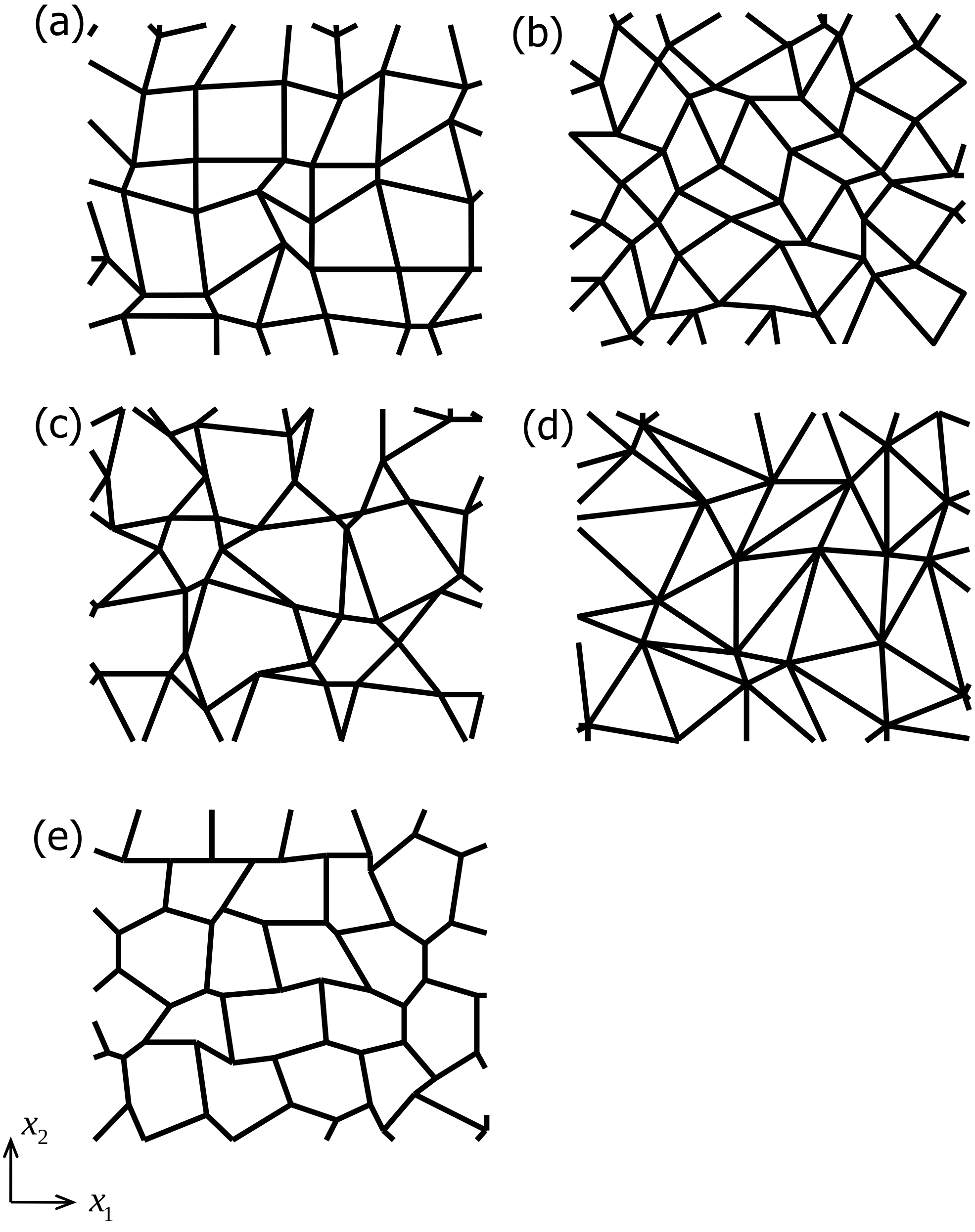

Fig. 2. Examples of the imperfect lattices ($R/\ell = 0.5$). (a) 0/90° square; (b) ±45° square; (c) Kagome lattice; (d) triangular honeycomb; (e) hexagonal honeycomb.

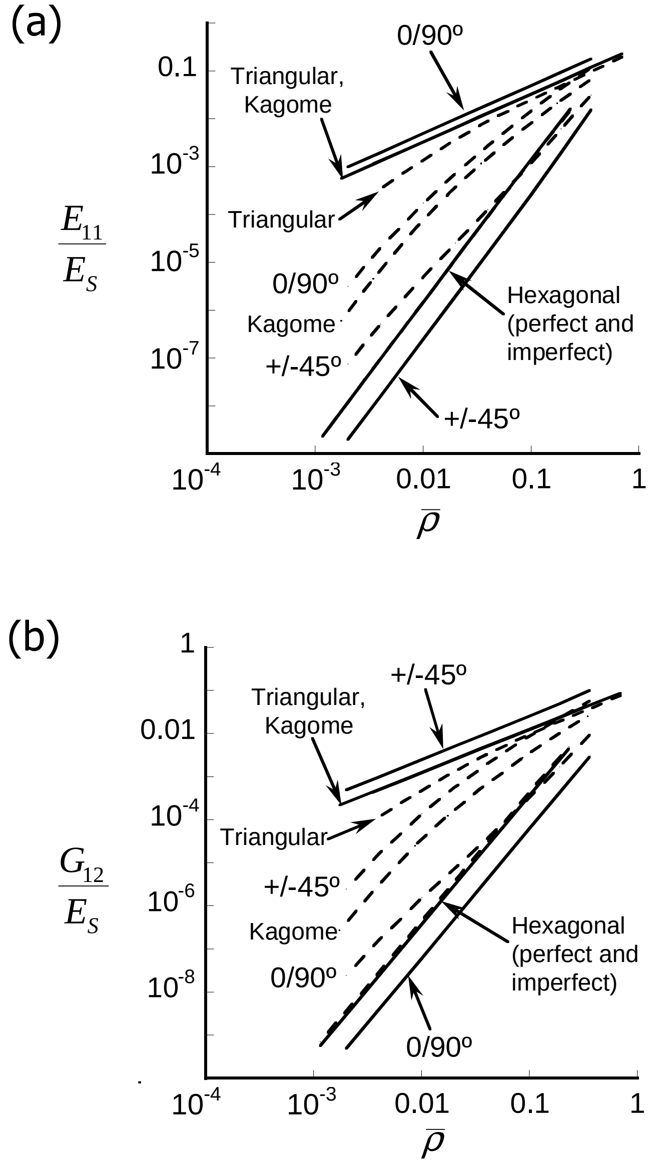

Fig. 3. Dependence of elastic moduli upon relative density $\overline{\rho}$ for perfect and imperfect lattices. (a) Direct modulus; (b) Shear modulus. The results for the perfect lattices ($R/\ell = 0$) are shown by solid lines, while results for imperfect lattices ($R/\ell = 0.5$) are shown by dashed lines.

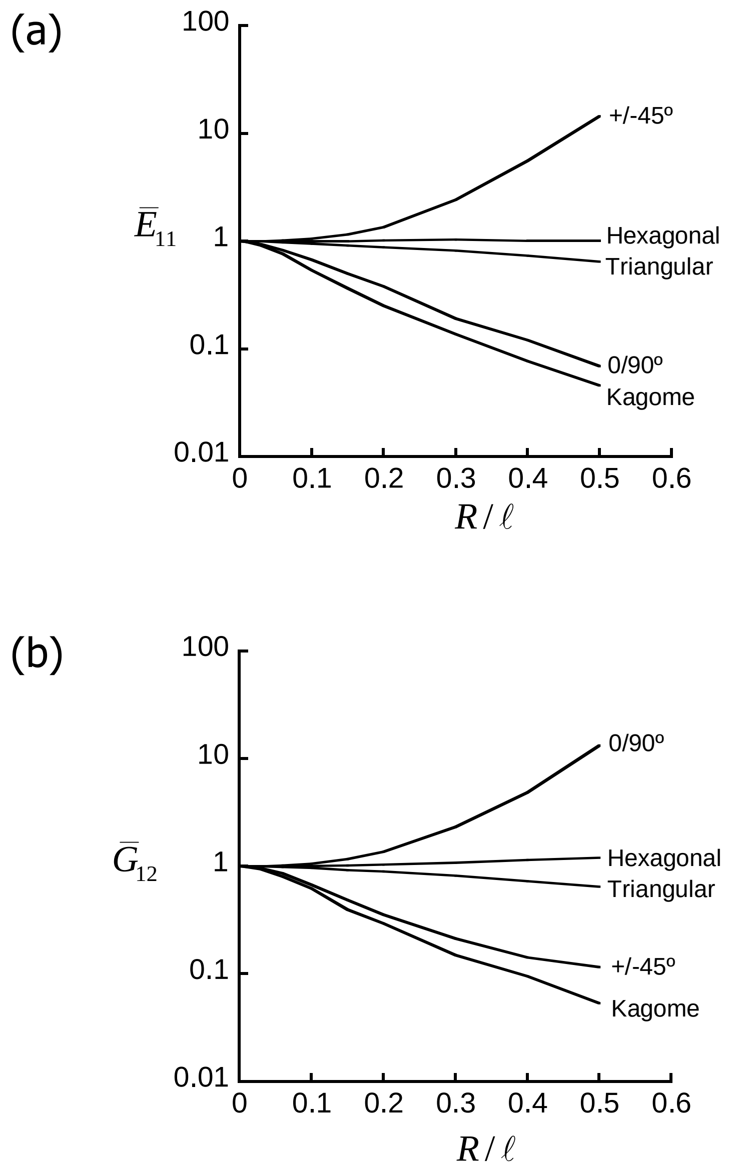

Fig. 4. Effect of imperfection R/ℓ upon elastic moduli at fixed $t/\ell = 0.01$. (a) Direct modulus; (b) Shear modulus.

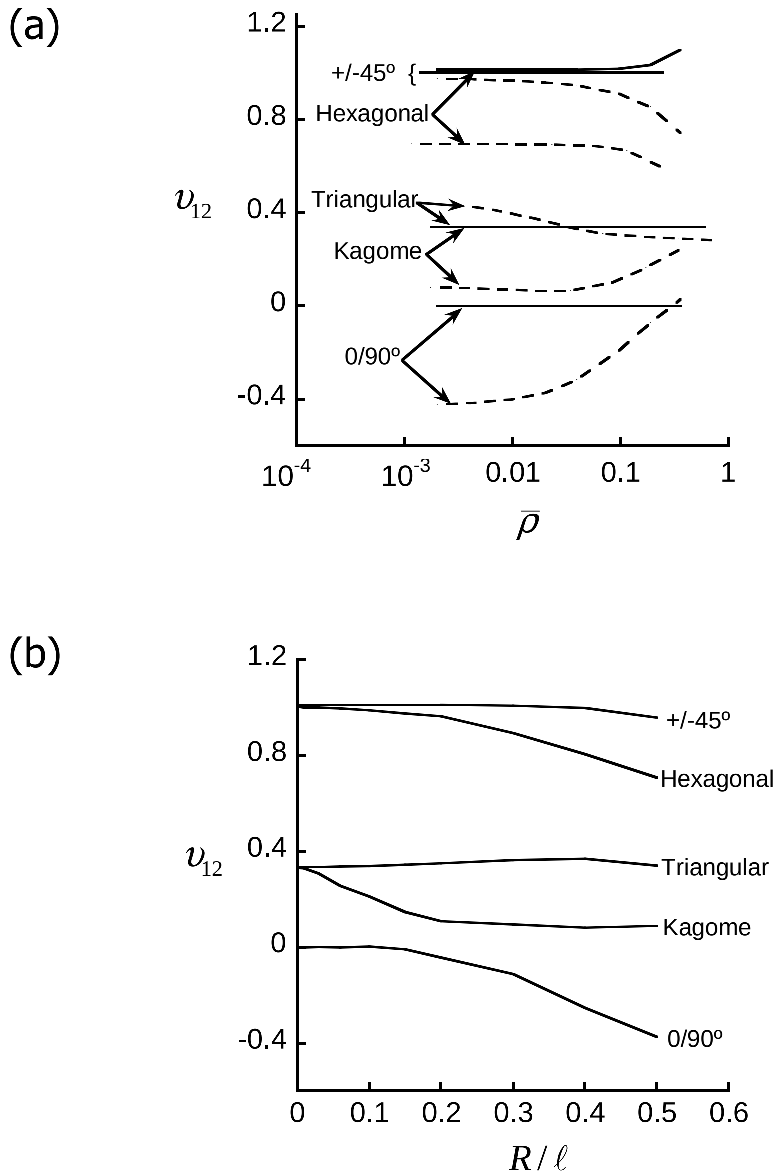

Fig. 5. Dependence of Poisson's ratio ν_{12} upon (a) $\overline{\rho}$; (b) R/ℓ. In (a), results for the perfect lattices ($R/\ell = 0$) are shown by solid lines, while results for imperfect lattices ($R/\ell = 0.5$) are shown by dashed lines. In (b), the aspect ratio is held fixed at $t/\ell = 0.01$.

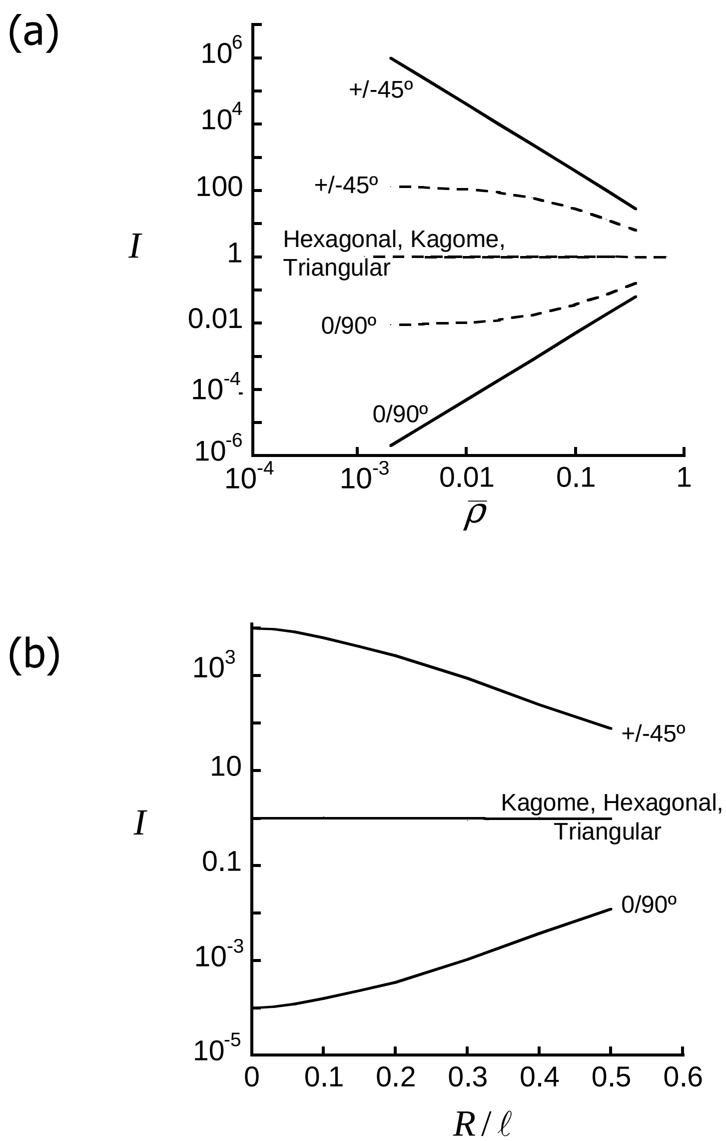

Fig. 6. The dependence of the anisotropy measure I upon (a) $\overline{\rho}$; (b) R/ℓ. In (a), solid lines denote $R/\ell = 0$ and dashed lines denote $R/\ell = 0.5$. In (b), t/ℓ equals 0.01.

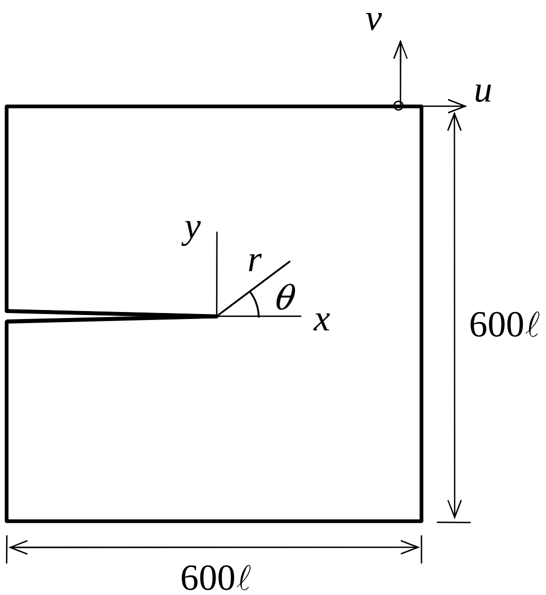

Fig. 7. The finite element mesh and crack tip co-ordinate system used in the fracture toughness predictions.

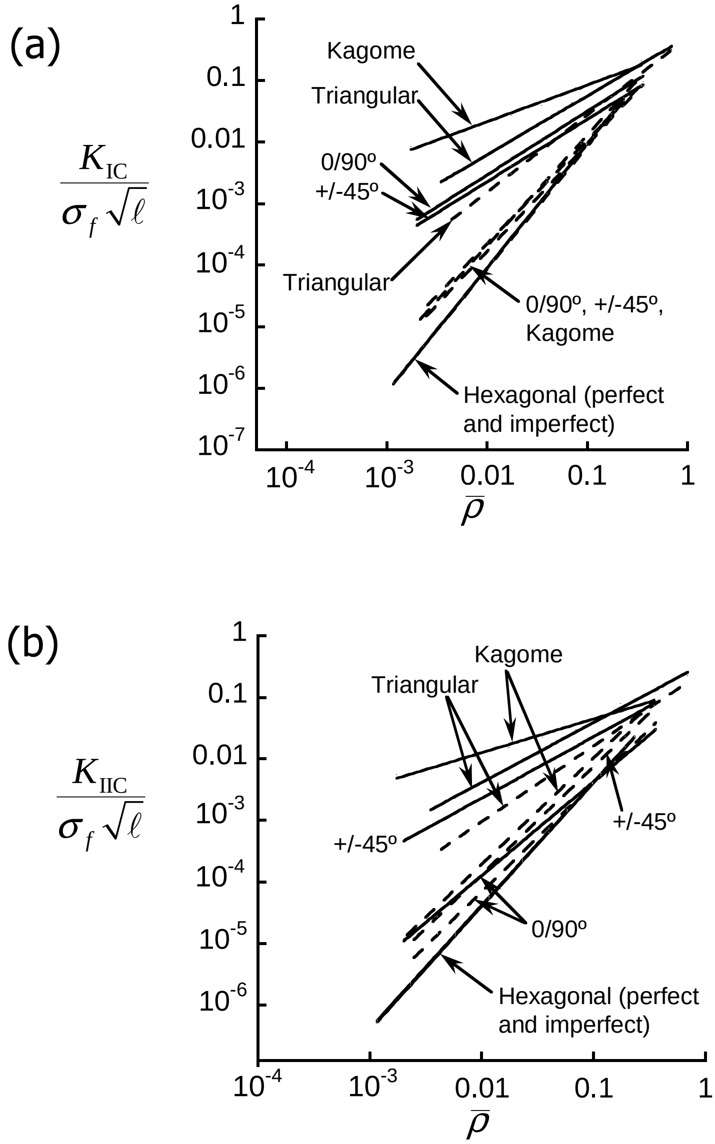

Fig. 8. Dependence of (a) mode I and (b) mode II fracture toughness upon $\overline{\rho}$. The solid lines represent $R/\ell = 0$ and the dashed lines represent $R/\ell = 0.5$.

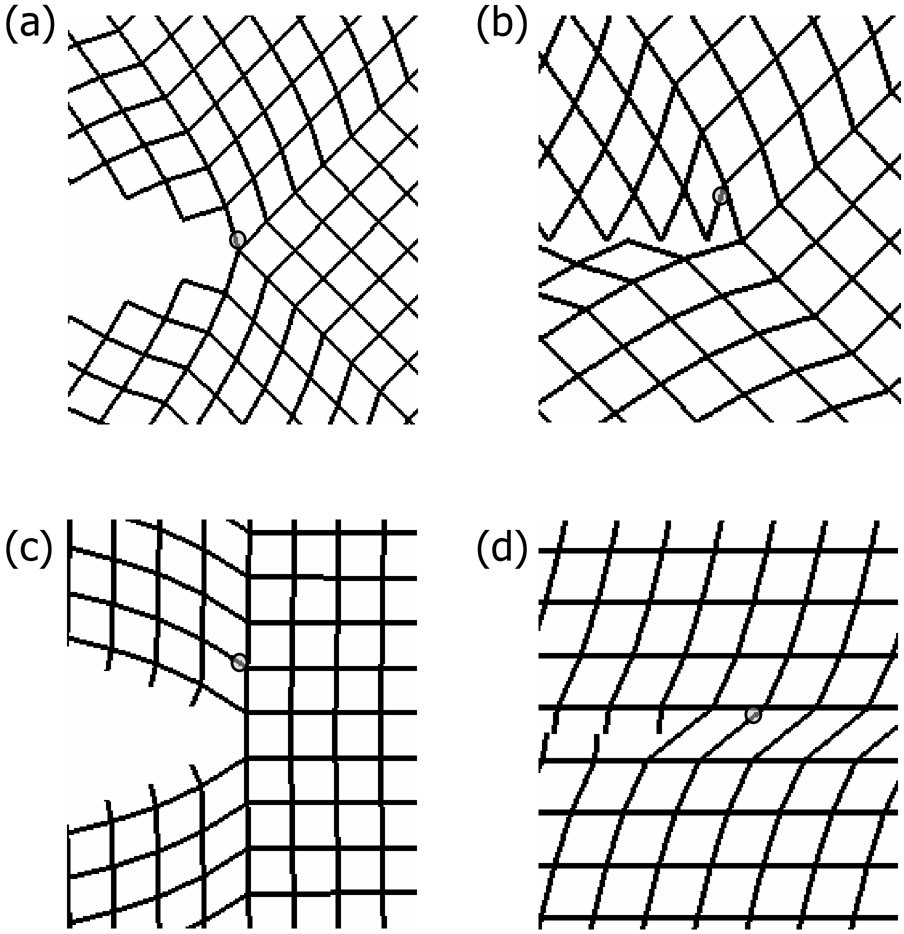

Fig. 9. Predicted failure location in $\pm 45°$ lattices under (a) mode I; (b) mode II loading, and in $0/90°$ lattices under (c) mode I and (d) mode II loading. The location is insensitive to the values of $\overline{\rho}$.

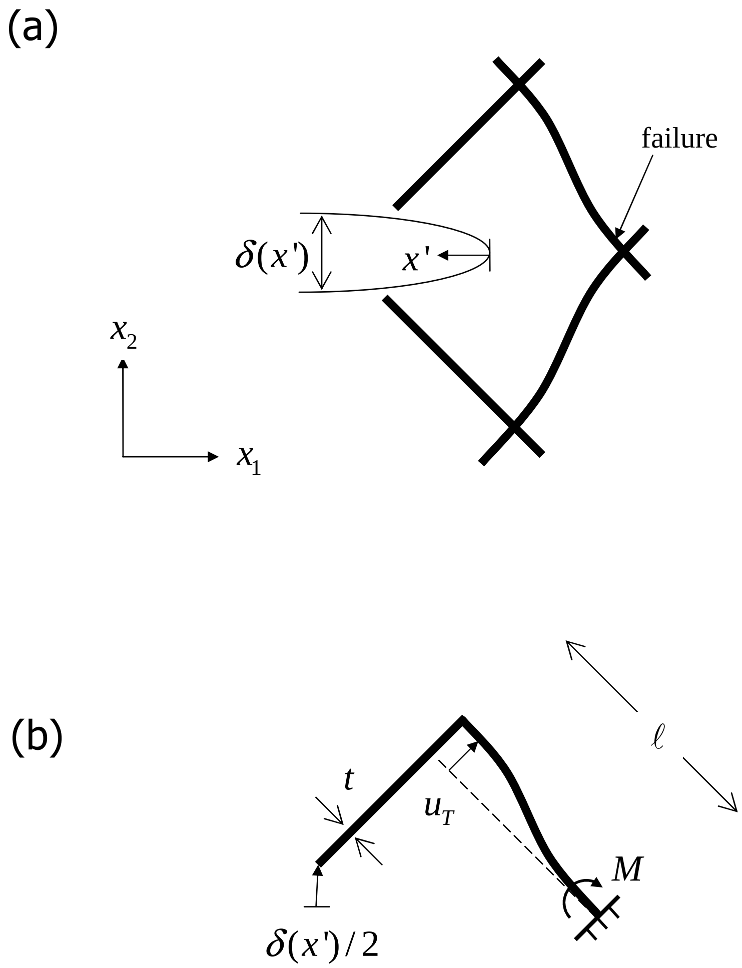

Fig. 10. (a) Deformation state at the crack tip of the ±45° lattice under mode I loading, (b) beam analysis of the critical bar.

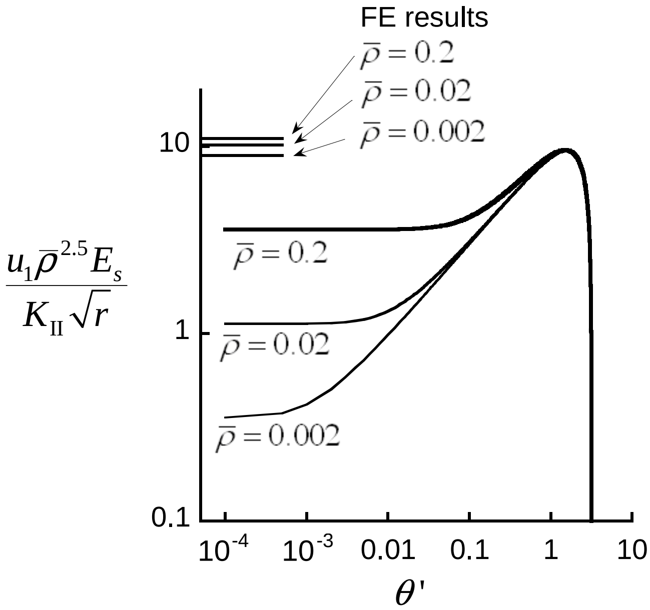

Fig. 11. The near tip displacement u_1 in an orthotropic elastic plate under mode II loading, plotted as a function of $\theta' \equiv \pi - \theta$.

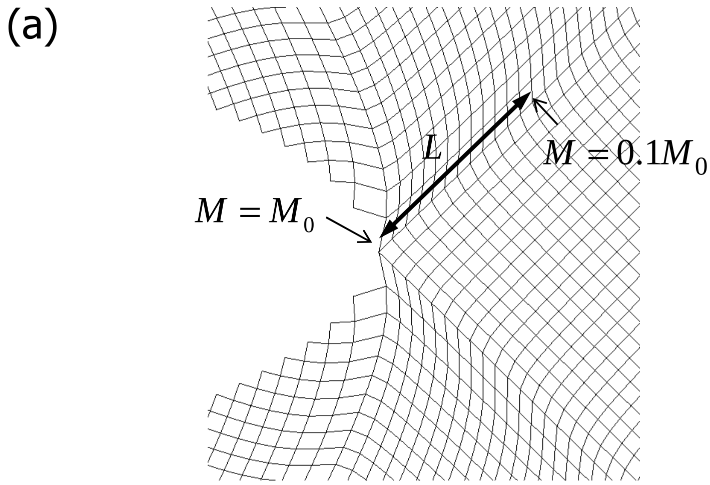

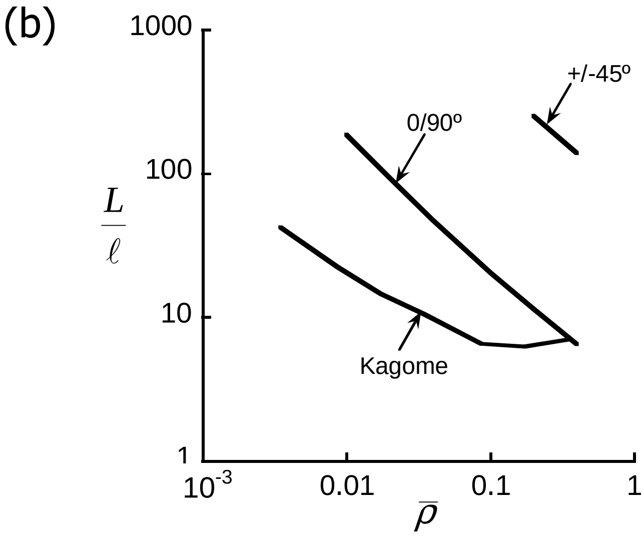

Fig. 12. (a) Deformed ±45° mesh under mode I loading, showing the length L of the shear lag region; (b) Dependence of L upon $\overline{\rho}$ for the square and Kagome lattices.

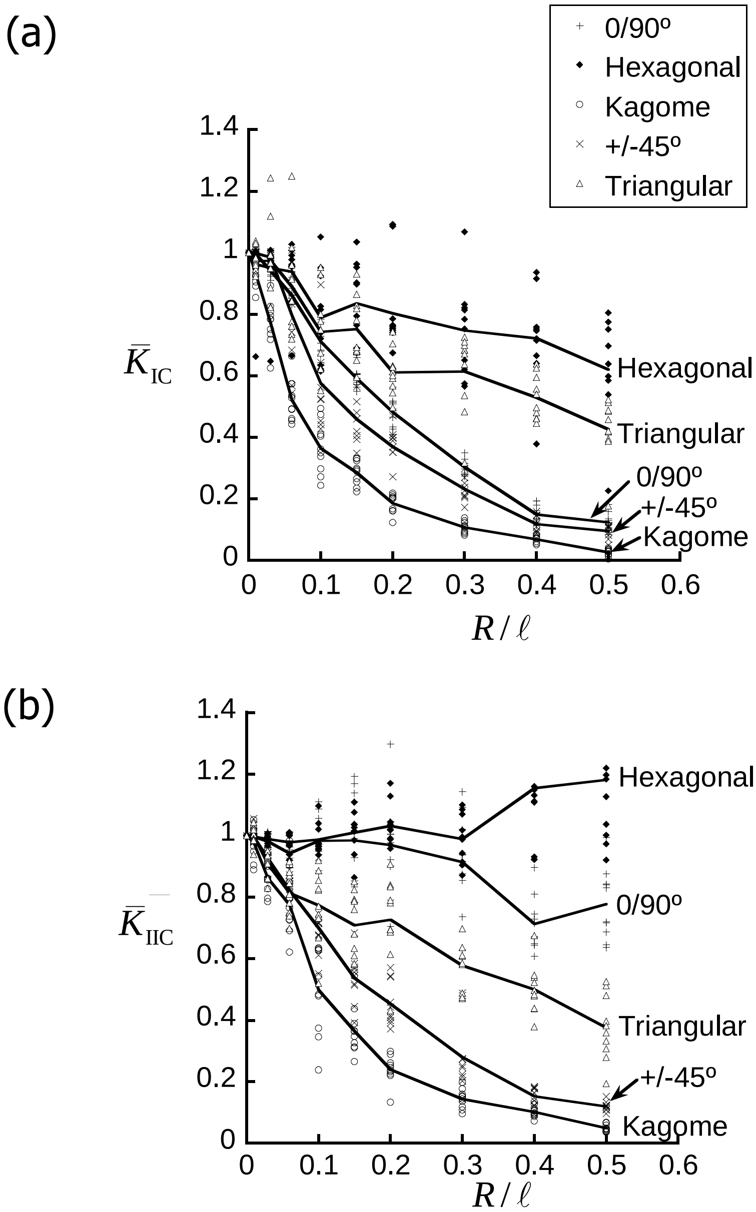

Fig. 13. Dependence of (a) normalised mode I fracture toughness and (b) normalised mode II fracture toughness upon R/ℓ, at $t/\ell = 0.01$.

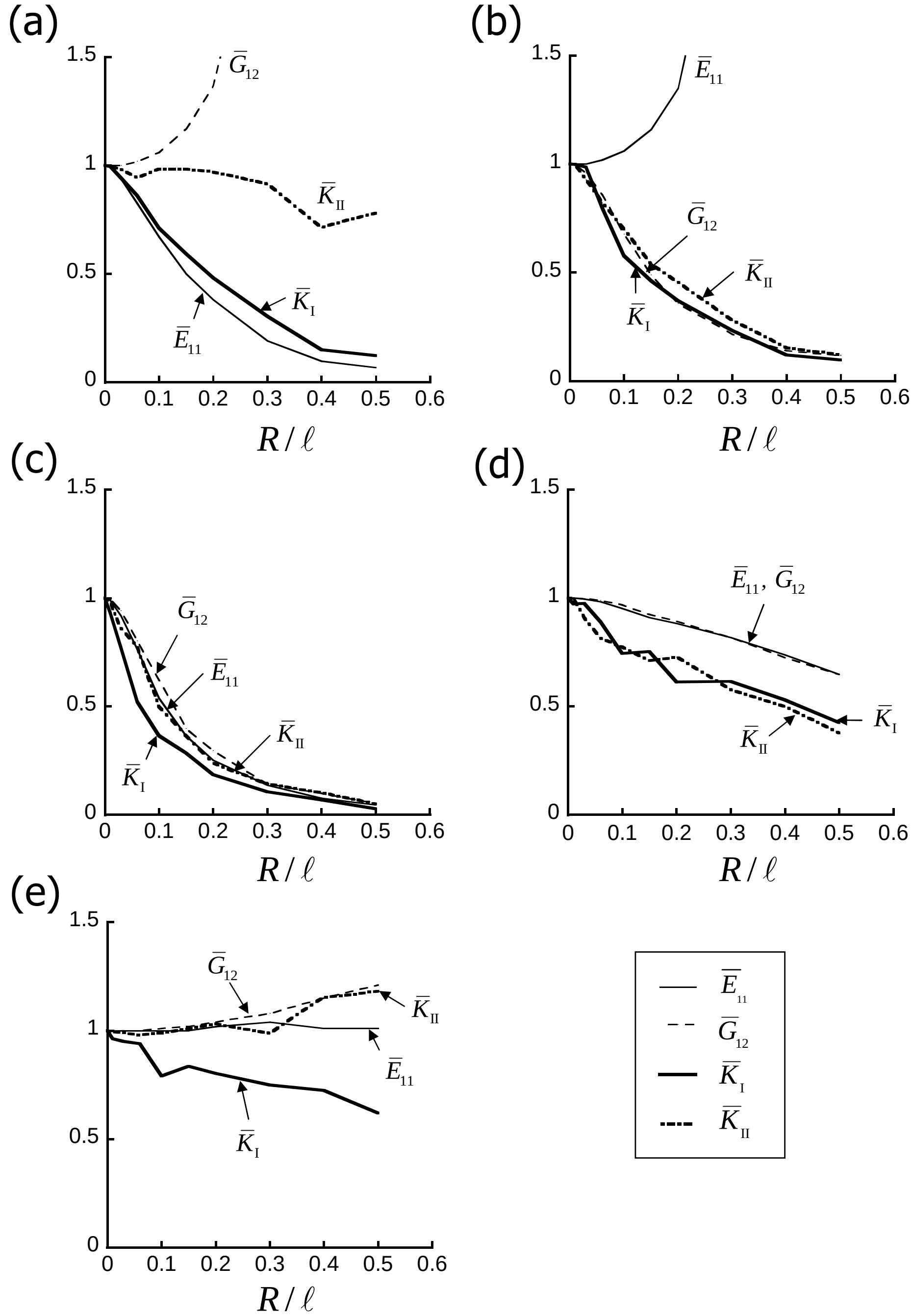

Fig. 14. Comparison of the imperfection sensitivity of modulus and fracture toughness, for lattices with $t/\ell = 0.01$. (a) 0/90° square lattice; (b) ±45° square lattice; (c) Kagome lattice; (d) triangular honeycomb; (e) hexagonal honeycomb.

	0/90°	±45°	Kagome	Triangular	Hexagonal
A	2	2	$\sqrt{3}$	$2\sqrt{3}$	$2/\sqrt{3}$
B	1/2	1/4	1/3	1/3	3/2
b	1	3	1	1	3
C	1/16	1/4	1/8	1/8	3/8
c	3	1	1	1	3
ν_{12}	0	1	1/3	1/3	1

Table 1
The in-plane elastic moduli of perfect lattices.

	0/90°	±45°	Kagome	Triangular	Hexagonal
E_{11}^{ps}	$\frac{2E_{11}}{2-\nu_s^2}$	$\frac{4E_{11}}{4-\overline{\rho}^2\nu_s^2}$	$\frac{3E_{11}}{3-\nu_s^2}$	$\frac{3E_{11}}{3-\nu_s^2}$	$\frac{2E_{11}}{2-3\overline{\rho}^2\nu_s^2}$
ν_{12}^{ps}	$\frac{\nu_s^2}{2-\nu_s^2}$	$\frac{4+\overline{\rho}^2\nu_s^2}{4-\overline{\rho}^2\nu_s^2}$	$\frac{1+\nu_s^2}{3-\nu_s^2}$	$\frac{1+\nu_s^2}{3-\nu_s^2}$	$\frac{2+3\overline{\rho}^2\nu_s^2}{2-3\overline{\rho}^2\nu_s^2}$

Table 2
The plane-strain elastic moduli of perfect lattices.

	Mode I		Mode II	
	D	d	D	d
0/90°	0.278	1	0.121	3/2
±45°	0.216	1	0.225	1
Kagome	0.205	1/2	0.115	1/2
Triangular	0.607	1	0.404	1
Hexagonal	0.902	2	0.408	2

Table 3
The fracture toughness of perfect lattice structures.

	Mode I		Mode II	
	D'	d'	D'	d'
Present study, Eq. (27)	0.185	1	0.089	5/4
Choi and Sankar (2005), fixed ℓ	0.039	1.05	0.137	1.32
Choi and Sankar (2005), fixed t	0.369	1.04	0.130	1.32

Table 4
The fracture toughness of perfect cubic lattices.